Alignment, calibration, and validation of an adaptive optics scanning laser ophthalmoscope optimized for resolving human cones in the central fovea

BENJAMIN MOON,[1,2,*] MARTINA POLETTI,[2,3,4] AUSTIN ROORDA,[5] PAVAN TIRUVEEDHULA,[5] SOH HANG LIU,[1,2] GLORY LINEBACH,[1,2] MICHELE RUCCI,[2,3] AND JANNICK P. ROLLAND[1,2,6]

[1]*The Institute of Optics, University of Rochester, Rochester, NY 14627, USA*
[2]*Center for Visual Science, University of Rochester, Rochester, NY 14627, USA*
[3]*Department of Brain and Cognitive Sciences, University of Rochester, Rochester, NY 14627, USA*
[4]*Department of Neuroscience, University of Rochester, Rochester, NY 14627, USA*
[5]*Herbert Wertheim School of Optometry and Vision Science, University of California Berkeley, Berkeley, CA 94720, USA*
[6]*Department of Biomedical Engineering, University of Rochester, Rochester, NY 14627, USA*
**b.moon@rochester.edu*

Abstract: Advances in adaptive optics scanning laser ophthalmoscope (AOSLO) technology have enabled cones in the human fovea to be reliably resolved, providing new insight into human foveal anatomy, visual perception, and retinal degenerative diseases. These high-resolution ophthalmoscopes require careful alignment of each optical subsystem to ensure diffraction-limited imaging performance, which is necessary for resolving the smallest foveal cones. We present a systematic and rigorous methodology for building, aligning, calibrating, and testing an AOSLO optimized for imaging the cone mosaic of the central fovea in humans. This methodology uses a two-stage alignment procedure and thorough system testing to achieve an AOSLO with diffraction-limited performance. Human retinal imaging of two healthy subjects demonstrates that the system can reliably resolve the smallest foveal cones.

© 2022 Optica Publishing Group under the terms of the Optica Publishing Group Open Access Publishing Agreement

1. Introduction

The use of adaptive optics in instrumentation for studying the human visual system has contributed to significant advances in understanding human retinal anatomy. Since the first use of adaptive optics in a retinal imaging system [1] and the subsequent application of adaptive optics to the scanning laser ophthalmoscope [2], the ability to compensate for the eye's monochromatic aberrations has proved essential for achieving cellular resolution of retinal structures in the living human eye. Recent advances in the adaptive optics scanning laser ophthalmoscope (AOSLO) have enabled the smallest cones in the human fovea to be reliably resolved, providing a means to investigate the characteristics of the cone mosaic—including cone density and its relationship to eye length, symmetries in the distribution of cones, and visual sensitivity at various foveal eccentricities—with unprecedented detail [3–8].

In addition to these studies investigating basic science questions about foveal anatomy in humans with normal vision, AOSLO systems with cellular resolution in the central fovea can provide key data for the detection and monitoring of retinal degenerative diseases. Foote *et al.* demonstrated that foveal cone density—measured with AOSLO—can decrease up to 42% below normal in subjects with a range of inherited retinal degenerations while visual acuity—measured with the Early Treatment of Diabetic Retinopathy Study protocol—remains at 20/20 or better [9]. This finding suggests that routine cone density measurements could be a vital tool

for early detection and monitoring of disease progression. Song *et al.* found that foveal cone density is significantly lower in the less-affected eye of patients with asymmetrical idiopathic macular telangiectasia (MacTel) when compared to the normal subject population, suggesting that cone density measurements could be useful for the detection and monitoring of MacTel [10]. A host of additional clinical applications for AOSLO systems with cellular resolution are surveyed in the recent review by Wynne *et al.* [11]. These promising clinical applications of AOSLO depend on hardware that can reliably resolve the smallest human foveal cones, which requires an optical system that has simultaneously a sufficiently large numerical aperture at the retina to meet the resolution requirement and is well-corrected to meet the diffraction limit.

While AOSLO systems provide great potential for both basic and translational research, the complexity of these systems and the lack of accessible procedures for their alignment and maintenance have contributed to restricting their use to specialized laboratories. Multiple afocal relay telescopes must be employed in AOSLO systems to achieve distortion-free scanning and reliable adaptive optics correction. These telescopes relay the entrance pupil of the system onto a fast (resonant) scanner, a slow (galvo) scanner, a deformable mirror, and the entrance pupil of the eye. Alignment errors in any of the telescopes can degrade the imaging performance by introducing optical aberrations. These residual system aberrations can often be corrected by the adaptive optics control loop, but this approach has the undesirable consequence of reducing the range of aberration correction that can be achieved by the deformable mirror when imaging the human retina. To achieve optimum image quality and performance over the large range of refractive errors and higher-order aberrations normally present across human observers, it is therefore desirable to have a well-aligned optical system. This is especially true in applications where cellular resolution in the central fovea is required because the diffraction-limited spot size for near-infrared imaging wavelengths is comparable to the smallest cone diameters.

Previous articles have described the optical, mechanical, and system design of AOSLO systems [2,3,12–15]. Less emphasis has, however, been given to the alignment and system validation procedures used during the implementation of these AOSLOs. Notable exceptions are provided by [16], which describes an active alignment strategy for minimizing the defocus after each relay telescope in the AOSLO, and by the recent work of Lu *et al.* presenting an approach for characterizing the performance of the completed AOSLO by imaging a three-bar resolution target [17]. However, there is a need for a comprehensive approach to AOSLO implementation that includes all aspects of assembly, alignment, and testing.

This paper presents rigorous alignment and system validation procedures for an AOSLO. Active alignment strategies are used to ensure that each relay telescope is properly aligned in an afocal configuration, with collimated input light yielding collimated output light. A portable Shack-Hartmann wavefront sensor is positioned at each intermediate pupil plane during fine alignment of the system, allowing the wavefront to be measured after each relay telescope. The wavefront sensor is also positioned at the eye pupil plane and the system exit pupil planes to verify that both the light delivery and light collection paths are diffraction-limited according to the Maréchal criterion (i.e., RMS wavefront error less than 0.07 waves at any wavelength of operation). Further system validation tests include imaging a distortion grid target to measure and digitally correct for the sinusoidal distortion from the resonant scanner and imaging a three-bar resolution target to quantify the system resolution. Finally, human retinal images are collected, demonstrating that the smallest cones at the center of the fovea are resolved.

2. Methods

2.1 System design and specifications

The design for the AOSLO used in this study is optimized for diffraction-limited performance over a 1-degree square field of view. The design closely resembles the system described in Mozaffari *et al.* [15]. The schematic for the system is shown in Fig. 1 and the specifications are listed in Table 1.

The system has four spectral channels with central wavelengths of 543 nm, 680 nm, 840 nm, and 940 nm. The 840 nm channel serves as the primary imaging channel, while the two visible channels (i.e., 680 nm and 543 nm) are used for stimulus delivery and possible future expansion in retinal imaging. The 940 nm channel is used for wavefront sensing. These four spectral channels are produced by dividing and spectrally filtering the broadband output from a supercontinuum fiber laser. The three imaging and stimulus delivery channels (i.e., 840 nm, 680 nm, and 543 nm) are modulated with acousto-optic modulators (AOMs), allowing the intensity of each channel to be independently adjusted and enabling stimuli to be drawn on the retina by embedding visible light patterns in the AOSLO raster scan. Fast scanning is achieved by a 15.5 kHz resonant scanner. Slow scanning uses a 30 Hz galvo scanner. The scanning field of view can be adjusted by changing the control voltages for each scanner. The optical design uses spherical mirrors in an off-axis and out-of-plane configuration to achieve an unobscured system with minimal astigmatism [3].

The adaptive optics control loop consists of a custom Shack-Hartmann wavefront sensor, a deformable mirror with 97 actuators, and custom software for wavefront control. When the adaptive optics control loop is running, the aberrations of the human eye are corrected, resulting in a diffraction-limited spot of light being scanned across the retina. Backscattered light then travels back through the scanning system and is separated into different spectral channels using dichroic filters in the detection arm. The light in each of the imaging channels is focused onto a sub-Airy-disk confocal pinhole by a focusing lens and then detected by a high-sensitivity photomultiplier tube (PMT).

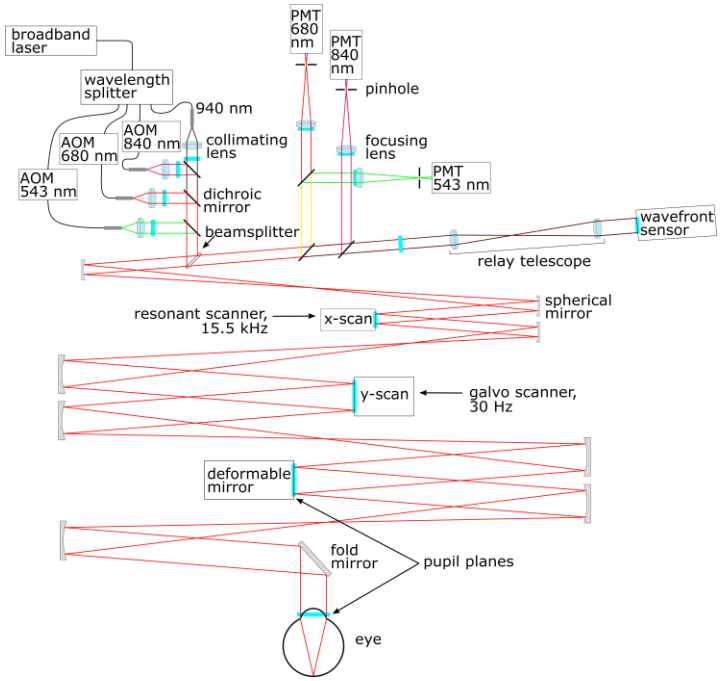

Fig. 1: Schematic for the AOSLO system showing the light delivery path, the scanning system, the detection arm, and the wavefront sensing arm. The pupil planes for the system are shown as cyan lines. The mirrors for each telescope are spherical, and they are arranged in a non-planar configuration to minimize astigmatism.

Table 1: System specifications for the AOSLO

System component	Specifications	Notes
Light source	Supercontinuum fiber laser, 470-2000 nm, 6 W output power	SuperK Extreme, EXR-20 (NKT Photonics A/S, Birkerød, Denmark)
Spectral filtering	543 ± 11, 680 ± 11, 840 ± 6, 940 ± 5 nm (FWHM)	Fiber-coupled wavelength splitting device with Thorlabs optomechanics and bandpass filters from Semrock
Acousto-optic modulators (AOMs)	0-50 MHz modulation, fiber-coupled AOMs	TEM-210-50-10-543/-680/-840-2FP-SM (Brimrose Corp., Sparks Glencoe, MD)
Horizontal scanner	15.5 kHz resonant scanner, Ø4.5mm active area	SC-30 (Electro-Optical Products Corp., Queens, NY) with custom mirror from Optimax
Vertical scanner	Galvanometer scanner, Ø9.5mm active area	6SD11170 (Cambridge Technology, Bedford, MA)
Photomultiplier tubes (PMTs)	Ø5 mm sensing area, 1 ns rise time, GaAs/GaAsP	H7422-40/-50 (Hamamatsu, Shizuoka Pref., Japan)
Amplifier for PMTs	0-50 MHz transimpedance amplifier, 25 mV/μA gain	C6438-01(Hamamatsu, Shizuoka Pref., Japan)
Confocal pinholes	Ø40/50 μm precision pinholes placed in front of PMTs	P40D/P50D (Thorlabs, Newton, New Jersey)
Wavefront sensor (WFS) camera	1.4 MP (1384 x 1032 pixels), 45 fps, 2/3" CCD	GS3-U3-15S5M-C (FLIR, Wilsonville, OR)
WFS lenslet array	200 μm pitch, 9 mm focal length, 12 x 12 mm size	APO-Q-P200-R4.15 (Advanced Microoptic Systems GmbH, Saarbrücken, Germany)
Deformable mirror	97 actuators, Ø7.2 mm pupil, 1.5 ms settling time	DM97-08 (ALPAO, Montbonnot, France)
Pupil diameter (at eye)	7.2 mm	Size set by deformable mirror aperture
Adaptive optics closed-loop frequency	15-25 Hz	-
Imaging frame rate	30 fps	-
Imaging field of view (FOV)	1 degree by 1 degree square	Measured in degrees of visual angle at the eye pupil plane
Imaging resolution	512 x 512 pixels, 8.53 pixels/arcmin @ 1° FOV	-

2.2 Coarse alignment strategy

A two-stage assembly and alignment procedure was used to efficiently install and align the components of the AOSLO while targeting the demanding imaging performance requirements. Section 2.2 describes the coarse alignment while Section 2.3 describes the fine alignment. Following the technique described in [15], a stencil containing all of the post locations on the optical table was generated from the optomechanical CAD model for the AOSLO. This stencil was laser cut in a thin acrylic sheet in two pieces and was then used to transfer the component post locations onto the optical table with a position uncertainty of +/- 1 mm. This approach simplified the coarse alignment procedure and enabled the system to be rapidly assembled on the optical table. The component heights were determined from the CAD model of the system and were realized by measuring the distance between the surface of the optical table and the corresponding reference plane on the mechanical mounts. Using this approach, each optical component was aligned in three dimensions with a position uncertainty of +/- 1 mm.

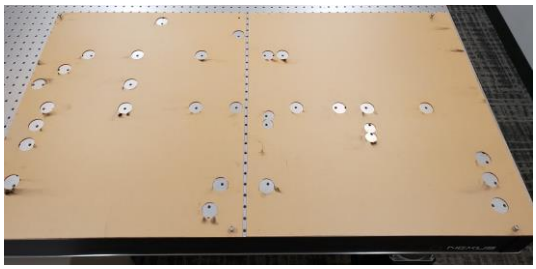

Fig. 2: Laser-cut stencil used to transfer the post coordinates onto the optical table during the assembly and coarse alignment of the AOSLO.

After aligning the position of each component on the optical table, the angle of each mirror in the scanning system was optimized to center the beam on the next mirror in the system. Precision-machined alignment guides (LMR1AP and LMR2AP from Thorlabs) were used to visualize the center of each spherical mirror (see Fig. 3). The 543 nm channel was used as the primary alignment channel because the green light could be easily seen at low power levels (i.e., less than 1 mW). Using the alignment guides, the beam was centered on each mirror in the beam path with an uncertainty of +/- 0.5 mm. This uncertainty corresponds to a maximum angular misalignment of +/- 7 arcmin for the mirror with the shortest optical path length to the next mirror. From conducting a tolerancing and sensitivity analysis of the AOSLO using optical design software, it was determined that the system would maintain diffraction-limited performance for misalignments of up to +/- 30 arcmin for this mirror. Therefore, the angular alignment attainable with the alignment guides is well within the alignment tolerance.

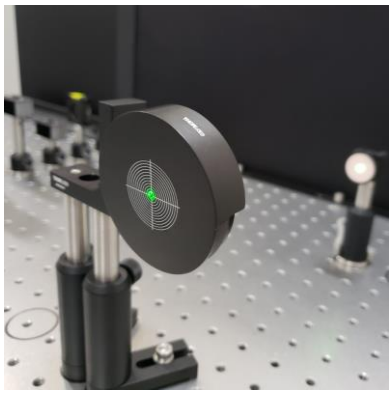

Fig. 3: Alignment guide used to center the laser beam on each of the spherical mirrors in the scanning system. Concentric circles surround a central hole, with a spacing of 1 mm between consecutive lines. Using these alignment guides, angular alignment better than +/- 7 arcmin can be achieved for each of the mirrors in the system. The laser beam from the 543 nm channel is shown being used to align a pair of mirrors in the scanning system.

2.3 Fine alignment strategy

After completing the coarse alignment, the portable Shack-Hartmann wavefront sensor (WFS40-7AR from Thorlabs) was sequentially placed at each intermediate pupil plane in the system during the fine alignment phase. This process required that the scanners and deformable mirror be temporarily removed to enable proper positioning of the wavefront sensor at the pupil planes. After using the wavefront sensor to verify that the incident wavefront was collimated at the entrance pupil plane for each of the four wavelength channels, the wavefront sensor was placed at the first intermediate pupil plane, corresponding to the fast scanner location. The

wavefront sensor was aligned to center the incident beam on the lenslet array and minimize tilt. Next, a wavefront measurement was collected, and the corresponding defocus was recorded. This initial measurement showed that there was 0.017 Diopters of defocus after the first telescope. As shown in Fig. 4, this measured defocus can be used to determine the required axial shift of mirror 2 to remove the residual defocus, as described by Eqs. (1) and (2).

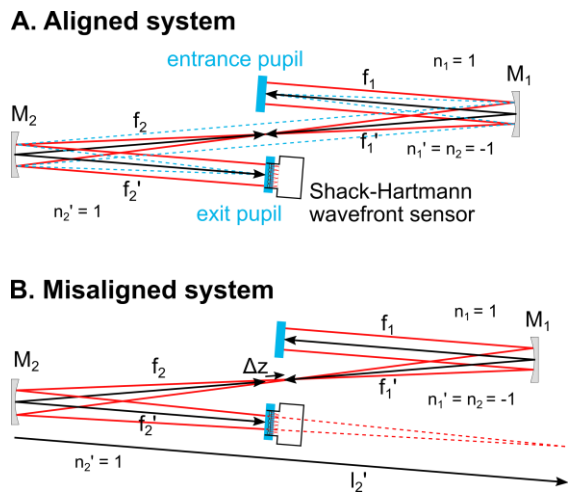

Fig. 4: Simplified schematic for a single telescope demonstrating the wavefront measurement and adjustment procedure. For the aligned system, the wavefront sensor at the exit pupil plane measures a collimated wavefront. For the misaligned system—where there is an axial positioning error for mirror 2—the wavefront at the exit pupil plane is converging or diverging. By measuring the wavefront curvature at the exit pupil plane, the axial shift required to correct for the measured defocus can be determined. As the position of mirror 2 is adjusted, the wavefront at the exit pupil plane is continuously measured until the residual defocus is reduced below the alignment tolerance.

$$\frac{n_2'}{l_2'} = \frac{n_2}{l_2} + \frac{n_2'}{f_2'} \tag{1}$$

$$l_2 = f_2 + \Delta z \tag{2}$$

Eq. (1) describes the thin-lens imaging properties of mirror 2, where n_2 and n_2' are the indices before and after mirror 2 respectively, l_2 is the object distance, l_2' is the image distance, and f_2' is the focal length of mirror 2. Eq. (2) shows that the object distance l_2 can be replaced by the sum of the front focal length, f_2, and the axial positioning error, Δz. The object distance, l_2', is determined from the wavefront measurement and is inversely proportional to the measured vergence, V_2', as shown in Eq. (3).

$$l_2' = \frac{n_2'}{V_2'} \tag{3}$$

Using Eqs. (1), (2), and (3), we can solve for the axial positioning error, Δz. Recalling that $f_2' = f_2$ for a mirror, we arrive at the simplified result shown in Eq. (4)

$$\Delta z = \frac{n_2 f_2'}{f_2' V_2' - n_2'} - f_2' \tag{4}$$

Plugging in the values corresponding to mirror 2 in the first telescope ($n_2 = -1$, $n_2' = 1$, $f_2' = 0.5$ m, $V_2' = 0.017$ D) we find that the measured defocus corresponds to an axial positioning error of 4.3 mm for mirror 2. After adjusting the position of mirror 2 by 4 +/- 1 mm (moving mirror 2 closer to mirror 1), the measured defocus at the exit pupil of the relay telescope was 0.008 Diopters, which is within the alignment tolerance of +/- 0.01 D. After optimizing the

spacing between mirrors 1 and 2, the fast scanner was reinstalled and its position along the optical axis was optimized by measuring along the optical axis from mirror 2 to the fast scanner and verifying that the distance was equal to the focal length of mirror 2. With the first telescope realigned and the fast scanner reinstalled, the beam angles were once again optimized before proceeding to the next telescope.

The procedures described above for the first telescope were repeated in each of the other three telescopes to ensure optimum alignment. First, the wavefront sensor was placed at the pupil plane after a given telescope and a wavefront measurement was taken. Then the required mirror shift along the optical axis was calculated and implemented. After making the position adjustment to the mirror and the wavefront sensor to ensure that the wavefront sensor remained at the pupil conjugate, another measurement was taken to verify that the mirror shift properly compensated for the residual defocus in the telescope. Mirror angles were then optimized for beam centration throughout the whole scanning system. Once all four telescopes were aligned using this procedure, wavefront measurements were taken at the eye pupil plane. It is important to note that the deformable mirror was replaced with a flat mirror (PF10-03-P01 from Thorlabs) during this fine alignment procedure to ensure that the resting shape of the deformable mirror would not introduce unknown defocus or aberrations into the system.

This active alignment technique—where a portable Shack-Hartmann wavefront sensor measures the wavefront shape and corresponding defocus at a pupil plane while adjustments are made to the axial position of a lens or mirror—was also utilized to install the relay telescope in front of the wavefront sensor, as pictured in Fig. 1. First, a flat mirror was placed at the eye pupil plane to reflect the incident light back through the scanners toward the detection channels. The portable wavefront sensor was then placed at the exit pupil plane to verify that there was good agreement between the wavefronts measured at the eye pupil plane and the exit pupil plane for the wavefront sensing channel. After verifying that the wavefront at the exit pupil was flat (less than +/- 0.01 D of defocus) and diffraction-limited (RMS wavefront error less than 0.07 waves), the two lenses that make up the relay telescope were installed. Measurements with a ruler were used to ensure that the first lens was positioned one focal length away from the pupil plane and the two lenses were separated by the sum of their focal lengths corresponding to an afocal relay telescope. Next, the portable wavefront sensor was placed at the exit pupil plane of the relay telescope. There was some residual defocus in the wavefront measurement at this plane, which was removed by adjusting the axial position of the second lens while monitoring the wavefront measured at the exit pupil plane.

2.4 System validation and testing

2.4.1 Wavefront measurements at the eye pupil plane

By using the fine alignment strategy described in Section 2.3, each telescope in the AOSLO was aligned to have less than +/- 0.01 Diopters of residual defocus. The portable Shack-Hartmann wavefront sensor was then placed at the eye pupil plane. Wavefront measurements at the eye pupil plane were collected for each of the four wavelengths used in the system. Again, the deformable mirror was removed from the system during these tests and replaced with a flat mirror to ensure that the resting shape of the deformable mirror would not contribute toward the measured wavefront. The beam diameter at the eye pupil plane is 7.2 mm, so all measurements were collected with a pupil diameter of 7.2 mm defined in the wavefront sensor software and a manually adjusted pupil offset to keep the measurement pupil centered on the beam. Raw wavefront maps were saved using the wavefront sensor software and were later analyzed in MATLAB. Results for the four wavelength channels are shown in Section 3.1.

Positioning the portable wavefront sensor at the eye pupil plane was also beneficial for fine-tuning the longitudinal chromatic aberration (LCA) that was introduced into the system to pre-compensate for the average LCA of the human eye. Inherent uncorrected LCA of the human eye would cause the four different wavelengths to focus at different retinal depths if all wavelengths were collimated at the eye pupil plane [18–20]. To account for the 1.2 Diopters of

LCA between the shortest and longest wavelengths used in the system (i.e., 543 nm and 940 nm, respectively), we employed the technique described in [15], where the distance between the input fiber tip and collimating lens was adjusted to introduce vergence for different spectral channels. With the 940 nm wavefront sensing channel being collimated (i.e., 0 Diopters of vergence), the input fiber for the 543 nm channel was moved 7.4 mm closer to the collimating lens—having a focal length of 40 mm—to introduce the required -1.2 Diopters of vergence at the eye pupil plane. By continuously monitoring the wavefront curvature at the eye pupil plane during these system adjustments, the correct amount of LCA was added to ensure that all wavelengths would focus at the same retinal plane for the average human eye.

2.4.2 Distortion grid measurements

Measurement and calibration of the field of view was conducted using a distortion grid target (R1L3S3P from Thorlabs). A model eye lens, consisting of a doublet lens (AC254-050-B from Thorlabs), was placed at the eye pupil plane. The distortion grid was aligned at the rear focal plane of the model eye lens. After installing the model eye, the adaptive optics control loop was enabled to compensate for any residual aberrations from the system or the model eye. Imaging was conducted with the 840 nm channel. The field of view in the AOSLO was adjusted by controlling the amplitude of the drive signals for the two scanners: the resonant scanner (i.e., horizontal) and the galvo scanner (i.e., vertical). Using the known grid spacing of the distortion grid (i.e., 50 μm grid spacing with +/- 1 μm spacing tolerance) and the focal length of the model eye lens, the full field of view in both the horizontal and vertical directions was determined from measurements of distortion grid images. Eq. (5) was used to compute the full field of view in either the horizontal or vertical direction: θ_{FFOV} is the horizonal (respectively vertical) full field of view, x (respectively y) is the measured width (or height) of the distortion grid image, and f' is the focal length of the model eye lens.

$$\theta_{FFOV} = 2\tan^{-1}\left(\frac{x}{2f'}\right) \tag{5}$$

Calibration curves for both the horizontal and vertical scanners were generated by adjusting the scanner amplitudes to achieve seven different square fields of view ranging from 0.13 degrees to 1.5 degrees for the full field of view. Distortion grid images for each of the seven measurements are shown in Fig. 5A. For the horizontal scanner, a cubic polynomial fit was used, while a quadratic polynomial fit was used for the vertical scanner. The measured data points and the polynomial fits are displayed in Fig. 5A, with red denoting the horizontal scanner and blue denoting the vertical scanner. The equations for the two polynomial fits are given by Eqs. (6) and (7), where H is the digital number for the horizontal scanner, θ_H is the horizontal full field of view in degrees, V is the digital number for the vertical scanner, and θ_V is the vertical full field of view in degrees.

$$H = (-83.9)\theta_H^3 + (283.0)\theta_H^2 + (100.0)\theta_H + (-8.8) \tag{6}$$

$$V = (20.0)\theta_V^2 + (71.7)\theta_V + (-0.5) \tag{7}$$

These calibration curves provide a means for determining the correct amplitude settings for the two scanners to achieve a desired field of view. For a 1-degree square full field of view—most commonly used in the retinal imaging experiments conducted with this AOSLO—the required amplitude settings are $H = 290$ and $V = 91$.

After calibrating the field of view and setting the scanner amplitudes to achieve a 1-degree square full field of view, a lookup table was generated to remove the sinusoidal distortion in the image caused by the horizontal scanner. The horizontal scanner is a resonant scanner, which oscillates at a frequency of 15.5 kHz. Its motion characteristics are sinusoidal, which causes the image to be stretched at the left and right edges of the frame and compressed near the center. The left image in Fig. 5B shows the distortion grid image before correcting for the sinusoidal distortion. Stretching at the right and left edges of the image is clearly visible. By quantifying

the location of each grid line in the image and comparing the real location to the expected location, the sinusoidal distortion can be corrected. A lookup table is then generated and used to resample the image pixels, which results in the distortion-free image in the right panel of Fig. 5B. This lookup table is then applied for real-time distortion correction in both the live and recorded videos.

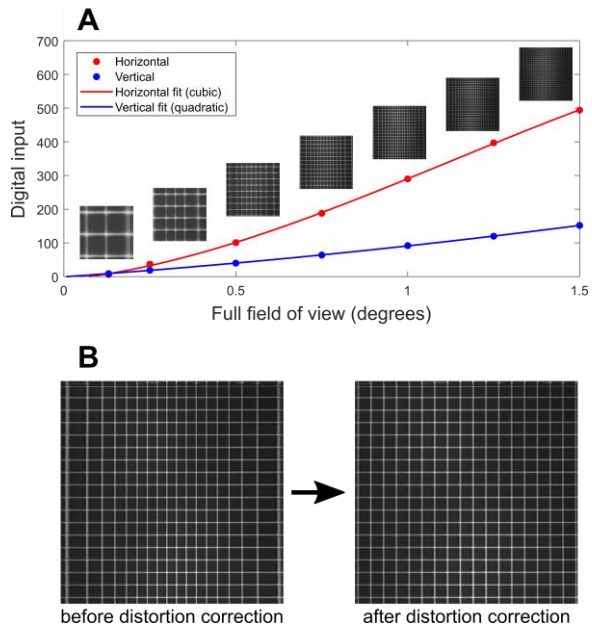

Fig. 5: A distortion grid was used to calibrate the field of view and correct for the sinusoidal distortion from the resonant scanner. A: images were taken at seven different square field of view settings and used to generate calibration curves for both the horizontal and vertical scanners. B: the distortion grid image on the left shows stretching at the edges of the frame due to the sinusoidal distortion from the resonant scanner. After distortion correction (right), the grid shows uniform spacing across the field of view.

2.4.3 Resolution target measurements

After calibrating the field of view and removing the sinusoidal distortion, a 1951 USAF three-bar resolution test target (R1DS1P from Thorlabs) was imaged to quantify the resolution limit of the completed AOSLO. The resolution target was placed at the back focal plane of the model eye lens and was imaged using the 840 nm channel. The resolution limits in both the horizontal and vertical directions were quantified as the maximum spatial frequency that could be resolved with all three bars clearly visible in the image. The measured resolution limits were then compared to the Rayleigh resolution limit for the imaging setup to demonstrate that the system could resolve features up to the diffraction limit. These results are shown in Section 3.2

2.4.4 Human retinal imaging

Retinal imaging was conducted for two young healthy subjects. The imaging protocols adhered to the ethical standards of the Research Subjects Review Board (RSRB) at the University of Rochester, and this study was approved by the RSRB at the University of Rochester. All subjects provided informed consent to participate in the study. One drop each of 1% tropicamide and 2.5% phenylephrine ophthalmic solutions were administered to one or both eyes of the subjects at least thirty minutes before the start of the imaging session. These eyedrops caused dilation of the pupil (mydriasis) and inhibition of accommodation (cycloplegia), which are necessary to achieve sufficient resolution and image quality during the

imaging session. Subjects sat in front of the AOSLO instrument and placed their chin on a chinrest. Temple pads were then adjusted to immobilize the head and maintain the subjects' position and stability in the system. A manual 3-axis translation stage was used to adjust the position of the head in the AOSLO to keep the eye pupil centered on the illumination beam.

During the imaging session, subjects fixated on a 4.7 x 4.7 arcmin dark square presented within the 60 x 60 arcmin imaging field of view. This fixation marker was generated by modulating the AOM for the 840 nm light, resulting in a faint red background with a small blinking dark square. The fixation marker was flashed at 3 Hz with a 50% duty cycle. Subjects were instructed to fixate on the dark square, which could be moved to any location within the imaging field of view for a given retinal recording. The power levels used during the imaging session were well below the retinal exposure limits set by the ANSI standard in Z136.1-2014 [21] (i.e., 167 μW for 840 nm (imaging) and 67 μW for 940 nm (wavefront sensing)). Imaging sessions were between 30 and 60 minutes in length.

Videos were recorded with the AOSLO at each of nine fixation points, with each video being ten seconds long. The blinking fixation marker was moved to each of the four corners, four edges, and the center of the square AOSLO raster scan. By using these multiple fixation points, a composite image spanning approximately 1.8 x 1.8 degrees on the retina was generated after registering each video and aligning the nine stabilized frames to a common reference. Additional details of the video and image processing techniques are described in Section 3.3.

3. Results

3.1 Wavefront measurements at the eye pupil plane

Wavefront measurements of the fully aligned light delivery system demonstrate that each of the four channels is diffraction-limited at the eye pupil plane. Fig. 6 shows the wavefront maps for each spectral channel. The RMS wavefront error is less than 0.05 waves for all channels, which is well below the Maréchal criterion for a diffraction-limited optical system (i.e., less than 0.07 waves). There is a small amount of residual astigmatism, coma, and higher-order aberrations present in the wavefront maps, but these residual aberrations have a negligible impact on the image quality because the resolution and image quality are primarily limited by diffraction. The peak-to-valley wavefront error is around 0.25 waves for all channels, with the 840 nm channel having the highest peak-to-valley wavefront error of 0.289 waves.

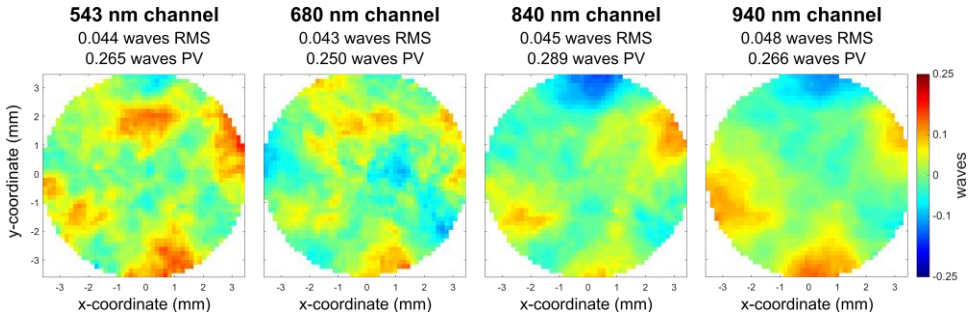

Fig. 6: Wavefront measurements at the eye pupil plane for each of the four spectral channels in the system. These results demonstrate that the system is well aligned and diffraction-limited according to the Maréchal criterion (i.e., RMS wavefront error less than 0.07 waves).

These measurements at the eye pupil plane validate the system alignment by showing that the combination of the individually aligned relay telescopes results in a diffraction-limited optical system. During the fine alignment of each relay telescope, the defocus was minimized, but other aberrations—such as astigmatism and coma—were not addressed. Combining the relay telescopes together in an out-of-plane configuration minimizes the overall system astigmatism [3], resulting in a diffraction-limited optical system. Resolving the smallest foveal

cones in the human retina requires this level of aberration correction. For the primary imaging wavelength of 840 nm and a standard 60 Diopter eye with a pupil diameter of 7.2 mm (i.e., the maximum pupil size attainable with this AOSLO), the Rayleigh resolution criterion for point-like objects is 2.4 µm. This means that objects separated by 2.4 µm on the human retina will be just resolved when the system is limited by diffraction. Since the minimum center-to-center spacing for human foveal cones is around 2.5 µm, the ability to resolve these smallest cones requires the optical system to be diffraction-limited. By ensuring that the aligned optical system meets this requirement, the full range of adaptive optics correction available with the deformable mirror can be applied to correct for the aberrations of the human eye.

3.2 Resolution measurements using a three-bar resolution target

Results from imaging a resolution target, shown in Fig. 7, further validate the system performance and demonstrate diffraction-limited imaging. Imaging was conducted over a 1-degree square field of view over a period of 10 seconds. The 300 captured frames were then averaged to obtain the image in Fig. 7A. The expanded view in Fig. 7B shows that features are clearly resolved up to group 7, element 2 for the horizontal axis and group 7, element 3 for the vertical axis. The Rayleigh resolution limit for this imaging configuration (i.e., wavelength of 840 nm, pupil diameter of 7.2 mm, and focal length of 50 mm) is 7.1 µm. This minimum feature separation for resolution corresponds to a maximum spatial frequency of 141 lp/mm. The spatial frequencies for elements 2 and 3 of group 7 are 144 and 161 lp/mm, respectively, which demonstrates that the imaging system can resolve features up to—and slightly beyond—the Rayleigh resolution criterion for a diffraction-limited optical system.

The small discrepancy between the resolution in the horizontal and vertical directions is a consequence of the scanning architecture. Residual jitter in the hsync signal can cause consecutive horizontal lines in the image to shift by +/- 1 pixel relative to the previous lines. When averaging across many frames, this horizontal jitter can reduce the contrast of the vertical bars used to quantify resolution along the horizontal axis. The horizontal jitter does not impact the contrast of the horizontal bars used to quantify vertical resolution because the direction of the jitter is along the length of the bars. This reasoning explains why the resolution for the red (vertical) line in Fig. 7B,C is higher than the resolution for the green (horizontal) line.

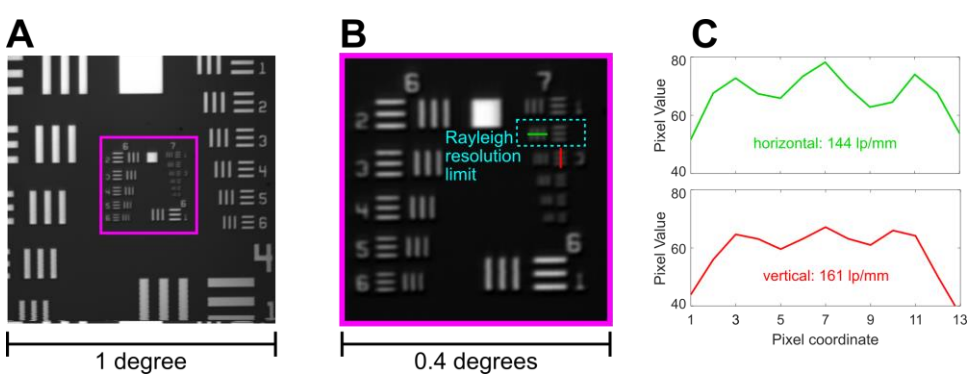

Fig. 7: A resolution target was placed at the back focal plane of a model eye lens and imaged with the 840 nm channel. The results demonstrate that the system can resolve features up to the Rayleigh resolution limit for the system. Imaging was conducted over a 1-degree square field of view, as shown in A. A close-up view of the central 0.4-degrees square is shown in B. Pixel value lineouts are shown in C for the maximum spatial frequency that is resolved for both the horizontal and vertical directions.

These results demonstrate that the system can collect high-resolution, diffraction-limited images over the 1-degree square field of view. Additional tests were conducted with the two visible imaging channels (i.e., 680 nm and 543 nm). Since these visible channels are used for

stimulus delivery rather than imaging the cone mosaic, they do not have the same diffraction-limited imaging requirement as the 840 nm channel. The 680 nm channel has a measured resolution of 203 lp/mm for horizontal and 144 lp/mm for vertical, while the diffraction-limited resolution is 174 lp/mm. The 543 nm channel has a measured resolution of 161 lp/mm for horizontal and 144 lp/mm for vertical, while the diffraction-limited resolution is 217 lp/mm. These results show that the visible channels achieve comparable resolution to the 840 nm channel but do not meet the diffraction-limited imaging criterion for both horizontal and vertical orientations. Future system optimizations will target to meet the diffraction-limited criterion for the visible channels by changing the zero-vergence wavelength to 680 nm instead of 940 nm. Making this adjustment will reduce the maximum vergence required to correct the average human LCA from -1.2 Diopters to -0.6 Diopters, which will lead to better image quality in the visible channels while still correcting for the 1.2 Diopters of LCA across the spectral range of the AOSLO.

3.3 Human retinal images

Human retinal images captured with the AOSLO demonstrate cellular resolution in the center of the fovea. 10-second videos were recorded at each of nine foveal locations. Each video was trimmed to approximately 100 frames in length, corresponding to the section of the video with the highest image quality and best fixation. Video frames were then processed using a strip-based image registration technique to compensate for the incessant involuntary eye movements that occurred during fixation. Following the technique described in [22–24], each video frame was divided into 32 horizontal strips, with each strip being 16 pixels in height. Strips were then cross correlated with a reference frame image to determine the shift for each strip. The computed shifts were then used to align the strips and construct stabilized frames. Once all video frames were stabilized, the frames were averaged to obtain a high-SNR image of the cone mosaic.

This image registration and stabilization procedure was conducted for each of the nine fixation points. The frame-averaged images were contrast enhanced and gamma corrected using ImageJ before making final adjustments to the brightness and contrast during the montage and stitch procedures. The resulting montaged composite images span approximately a 1.8-degree square centered near the preferred locus of fixation. Images from the two subjects who participated in this study are displayed in Fig. 8, with subpanels A and C showing the retinal montages and subpanels B and D showing a magnified region with the highest cone density.

These results demonstrate that the smallest foveal cones are resolved for both subjects. Preliminary cone density analysis on these images, following procedures similar to [7], yield peak cone densities of 12,826 cones per square degree for Z055 and 13,276 cones per square degree for Z160. These values are within the range of normal peak cone densities reported in the literature: 11,999 – 19,001 cones per square degree for [5] and 10,823 – 18,023 cones per square degree for [7]. A summary of the subject information is shown in Table 2. Both subjects who participated in this study were myopic, with spherical refractions of -2.0 and -3.5 Diopters. For subject Z055, the maximum pupil diameter over which the adaptive optics correction could be achieved was 6.5 mm, even after dilation. This smaller pupil diameter corresponds to a slight decrease in resolution, but the central foveal cones were still resolved for this subject, as Fig. 8D demonstrates.

Table 2: Data for human subjects who participated in the system evaluation study

Subject ID	Age	Eye Imaged	Spherical Refraction (D)	Pupil diameter (mm)
Z055	27	R	-3.5	6.5
Z160	28	R	-2.0	7.2

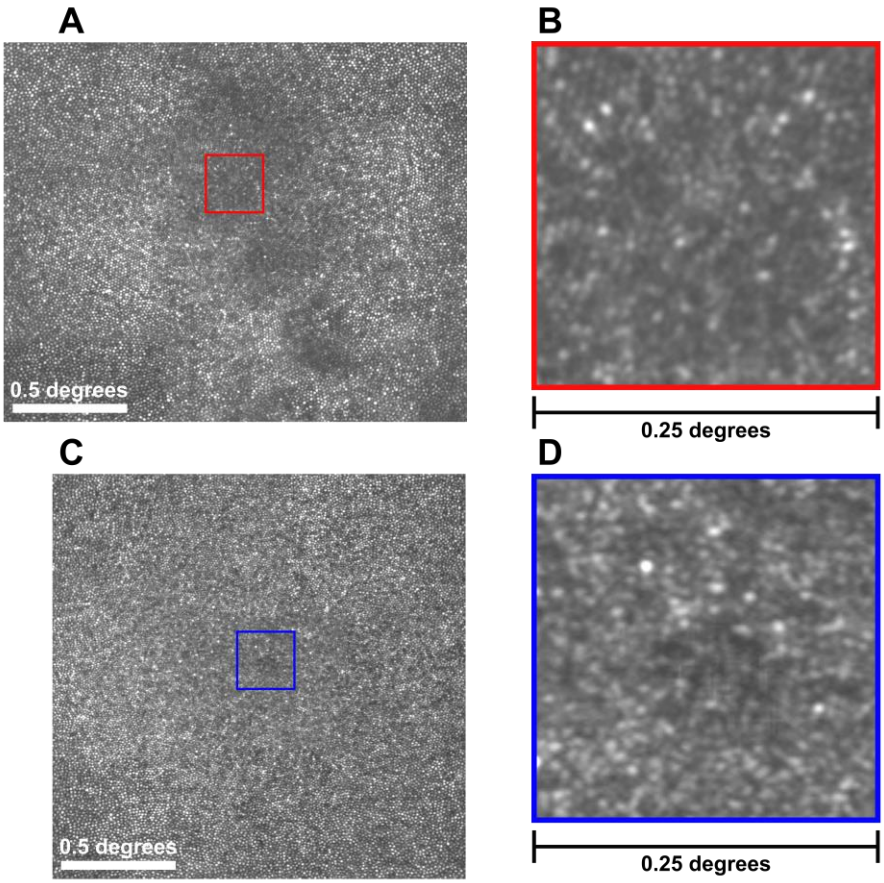

Fig. 8: Images of the human photoreceptor mosaic at the center of the fovea for two subjects collected with the aligned and optimized AOSLO using 840 nm illumination. Retinal montages (A and C) were generated by aligning and stitching images from nine different fixation points. Magnified views (B and D) show the retinal regions with the highest cone density over a 0.25-degree square. The smallest foveal cones are resolved for both subjects.

4. Conclusion

Implementing an AOSLO optimized for resolving the smallest human foveal cones requires a well-aligned optical system. This paper outlines rigorous alignment, calibration, and validation procedures for AOSLO systems. Starting with a CAD model for the system and a laser-cut stencil, the coordinates for each optical component and corresponding mechanical mount were transferred to an optical table, enabling rapid assembly and coarse alignment of the optical system. Following this coarse alignment, an active alignment strategy utilizing a portable Shack-Hartmann wavefront sensor was employed to correct for residual defocus in each of the afocal relay telescopes. By measuring the wavefront curvature at intermediate pupil planes and using principles and equations from first-order optics, the required axial shifts necessary to correct the residual defocus were determined and implemented.

Following this two-stage alignment procedure, various validation and calibration experiments were conducted to demonstrate the performance of the completed system. Wavefront measurements at the eye pupil plane demonstrated diffraction-limited performance for each of the four spectral channels. The wavefront sensor was then used to verify that the correct amount of defocus had been added to each channel to compensate for the longitudinal

chromatic aberration of the human eye. Images of a distortion grid target were used to calibrate the scanning field of view and digitally correct for the sinusoidal distortion from the resonant scanner. Images of a resolution test target enabled the quantification of the system resolution, demonstrating that diffraction-limited imaging was obtained for the primary imaging wavelength of 840 nm. Finally, human retinal imaging was conducted to demonstrate that the smallest foveal cones can be resolved in healthy subjects with normal vision.

The procedures described above provide a systematic approach for implementing AOSLO systems with optimum image quality. This approach is especially valuable for resolving cones in the central fovea because of the need for diffraction-limited imaging performance. By measuring and quantifying performance metrics—such as diopters of residual defocus or RMS wavefront error—during the alignment of the AOSLO, each optical subsystem can be individually optimized, resulting in a well-aligned and high-performing completed system. While AOSLO systems can provide excellent resolution and image quality of human retinal structures, these systems have not yet been commercialized or widely adopted in clinical practice, likely due to the challenges in system alignment and calibration. By describing a set of procedures covering many aspects of the system implementation and validation of an AOSLO, this work seeks to enable additional research groups to build AOSLOs and incorporate high-resolution human retinal imaging into their research efforts. The methods described in this paper were developed for applications where cellular resolution at the center of the fovea is necessary, but other AOSLO systems with less stringent resolution requirements—e.g., imaging over a larger field of view or outside of the fovea—will also benefit from the rigorous and systematic alignment and validation procedures presented.

The AOSLO described in this paper is currently being used in a human retinal imaging study investigating the relationships between anatomical features of the cone photoreceptor mosaic and oculomotor behavior. Given the high quality of the images captured with this system, the cone locations can be reliably marked using a semi-automated cone detection procedure [25]. Cone density analysis is then conducted to map the cone density across the fovea and determine the location of the peak cone density relative to the preferred retinal locus of fixation (PRL), which is identified by measuring the average position of each stimulus presentation on the retina from the recorded videos. These features of retinal anatomy will then be compared to oculomotor behavior data measured with a custom high-resolution digital Dual Purkinje Image eye tracker [26]. This ongoing study seeks to discover links between anatomical features of the human fovea—such as peak cone density or offset between the PRL and peak density location—and eye movement behavior to elucidate the mechanisms responsible for high-acuity vision.

Funding

Funding for this research was provided by NIH grants EY029788 and EY018363. Dissemination of UC Berkeley's AOSLO design and software was provided through the Resources Sharing Plan of EY023591.

Acknowledgements

The authors would like to acknowledge Ashley M. Clark, Sanjana Kapisthalam, Samantha K. Jenks, and Edith Hartmann for their assistance during the human retinal imaging sessions. We thank Sanam Mozaffari and Francesco LaRocca at UC Berkeley for making Zemax and SolidWorks designs of the AOSLO system available. William S. Tuten at UC Berkeley provided some custom hardware necessary to assembly the AOSLO. The Center for Visual Science at the University of Rochester provided resources and expertise valuable for completing this research, especially Martin Gira and Daniel Guarino for fabricating custom mechanical components and Karteek Kunala for advice on optical alignment techniques. Mike Pomerantz helped with the laser-cut stencil and the assembly of the custom Shack-Hartmann wavefront sensor. We thank Synopsys, Inc. for the student license of CODE V.

Disclosures

The authors declare that there are no conflicts of interest related to this article.

Data availability

Data files underlying the results in this paper are available upon reasonable request.

References

1. J. Liang, D. R. Williams, and D. T. Miller, "Supernormal vision and high-resolution retinal imaging through adaptive optics," J. Opt. Soc. Am. A **14**(11), 2884 (1997).
2. A. Roorda, F. Romero-Borja, W. J. I. Donnelly, H. Queener, T. J. Hebert, and M. C. W. Campbell, "Adaptive optics scanning laser ophthalmoscopy," Opt. Express **10**(9), 405–412 (2002).
3. A. Dubra and Y. Sulai, "Reflective afocal broadband adaptive optics scanning ophthalmoscope," Biomed. Opt. Express **2**(6), 1757 (2011).
4. M. A. Wilk, A. M. Dubis, R. F. Cooper, P. Summerfelt, A. Dubra, and J. Carroll, "Assessing the spatial relationship between fixation and foveal specializations," Vision Research **132**, 53–61 (2017).
5. Y. Wang, N. Bensaid, P. Tiruveedhula, J. Ma, S. Ravikumar, and A. Roorda, "Human foveal cone photoreceptor topography and its dependence on eye length," eLife **8**, e47148 (2019).
6. J. A. Cava, M. T. Allphin, R. R. Mastey, M. Gaffney, R. E. Linderman, R. F. Cooper, and J. Carroll, "Assessing Interocular Symmetry of the Foveal Cone Mosaic," Invest. Ophthalmol. Vis. Sci. **61**(14), 23 (2020).
7. J. L. Reiniger, N. Domdei, F. G. Holz, and W. M. Harmening, "Human gaze is systematically offset from the center of cone topography," Current Biology **31**(18), (2021).
8. N. Domdei, J. L. Reiniger, F. G. Holz, and W. M. Harmening, "The Relationship Between Visual Sensitivity and Eccentricity, Cone Density and Outer Segment Length in the Human Foveola," Invest. Ophthalmol. Vis. Sci. **62**(9), 31 (2021).
9. K. G. Foote, P. Loumou, S. Griffin, J. Qin, K. Ratnam, T. C. Porco, A. Roorda, and J. L. Duncan, "Relationship Between Foveal Cone Structure and Visual Acuity Measured With Adaptive Optics Scanning Laser Ophthalmoscopy in Retinal Degeneration," Invest. Ophthalmol. Vis. Sci. **59**(8), 3385 (2018).
10. H. Song, E. A. Rossi, and D. R. Williams, "Reduced foveal cone density in early idiopathic macular telangiectasia," BMJ Open Ophth **6**(1), e000603 (2021).
11. N. Wynne, J. Carroll, and J. L. Duncan, "Promises and pitfalls of evaluating photoreceptor-based retinal disease with adaptive optics scanning light ophthalmoscopy (AOSLO)," Progress in Retinal and Eye Research **83**, 100920 (2021).
12. K. Grieve, P. Tiruveedhula, Y. Zhang, and A. Roorda, "Multi-wavelength imaging with the adaptive optics scanning laser Ophthalmoscope," Opt. Express **14**(25), 12230 (2006).
13. A. Gómez-Vieyra, A. Dubra, and D. Malacara-Hernández, "First-order design of off-axis reflective ophthalmic adaptive optics systems using afocal telescopes," Opt. Express **17**(21), 18906 (2009).
14. J. Zhang, Q. Yang, K. Saito, K. Nozato, D. R. Williams, and E. A. Rossi, "An adaptive optics imaging system designed for clinical use," Biomed. Opt. Express **6**(6), 2120 (2015).
15. S. Mozaffari, F. LaRocca, V. Jaedicke, P. Tiruveedhula, and A. Roorda, "Wide-vergence, multi-spectral adaptive optics scanning laser ophthalmoscope with diffraction-limited illumination and collection," Biomed. Opt. Express **11**(3), 1617 (2020).
16. S. J. Steven, "Optical Design of Translational Broadband Reflective Adaptive Optics Ophthalmoscopes," University of Rochester (2020).
17. R. Lu, N. Aguilera, T. Liu, J. Liu, J. P. Giannini, J. Li, A. J. Bower, A. Dubra, and J. Tam, "In-vivo sub-diffraction adaptive optics imaging of photoreceptors in the human eye with annular pupil illumination and sub-Airy detection," Optica **8**(3), 333 (2021).
18. D. A. Atchison and G. Smith, "Chromatic dispersions of the ocular media of human eyes," J. Opt. Soc. Am. A **22**(1), 29 (2005).
19. M. Vinas, C. Dorronsoro, D. Cortes, D. Pascual, and S. Marcos, "Longitudinal chromatic aberration of the human eye in the visible and near infrared from wavefront sensing, double-pass and psychophysics," Biomed. Opt. Express **6**(3), 948 (2015).
20. X. Jiang, J. A. Kuchenbecker, P. Touch, and R. Sabesan, "Measuring and compensating for ocular longitudinal chromatic aberration," Optica **6**(8), 981 (2019).
21. *American National Standard for Safe Use of Lasers*, Safe Use of Lasers (Laser Institute of America, 2014).
22. S. B. Stevenson and A. Roorda, "Correcting for miniature eye movements in high-resolution scanning laser ophthalmoscopy," in *Ophthalmic Technologies XV* (SPIE, 2005), **5688**, p. 145.
23. D. W. Arathorn, Q. Yang, C. R. Vogel, Y. Zhang, P. Tiruveedhula, and A. Roorda, "Retinally stabilized cone-targeted stimulus delivery," Opt. Express **15**(21), 13731 (2007).
24. Q. Yang, D. W. Arathorn, P. Tiruveedhula, C. R. Vogel, and A. Roorda, "Design of an integrated hardware interface for AOSLO image capture and cone-targeted stimulus delivery," Opt. Express **18**(17), 17841 (2010).
25. K. Y. Li and A. Roorda, "Automated identification of cone photoreceptors in adaptive optics retinal images," J. Opt. Soc. Am. A **24**(5), 1358 (2007).
26. M. Rucci, R.-J. Wu, and Z. Zhao, "System and method for real-time high-resolution eye-tracking," United States patent US11003244B2 (May 11, 2021).